

<https://doi.org/10.1038/s42005-025-02052-x>

Nonequilibrium regimes for quasiparticles in superconducting qubits with gap-asymmetric junctions

Check for updates

Giampiero Marchegiani ¹✉ & **Gianluigi Catelani** ^{1,2}

Superconducting qubits hold promise for quantum computing, but their operation is challenged by various sources of noise, including excitations known as quasiparticles. Qubits with gap asymmetry larger than their transition energy are less susceptible to quasiparticle decoherence as the quasiparticles are mostly trapped in the low-gap side of the junction. Because of this trapping, the gap asymmetry can contribute to maintaining the quasiparticles out of equilibrium. Here we address the temperature dependence of the quasiparticle densities in the two sides of the junction. We show that four qualitatively different regimes are possible with increasing temperature: (i) nonequilibrium, (ii) local quasiequilibrium, (iii) global quasiequilibrium, and (iv) full equilibrium. We identify shortcomings in assuming global quasiequilibrium when interpreting experimental data, highlighting how measurements in the presence of magnetic field can aid the accurate determination of the junction parameters, and hence the identification of the nonequilibrium regimes.

Superconducting qubits are intensively investigated for quantum computing purposes¹. Despite tremendous improvement in performances over the last two decades, still more work is needed for the precise determination and the mitigation of qubit decoherence processes², which are necessary to realize a fault-tolerant large-scale quantum processor. Bogoliubov quasiparticles, the fundamental excitations in superconductors, couple to the qubit when tunneling across Josephson junctions, leading to decoherence^{3–5} and limiting the fidelity of some two-qubit gates⁶. Moreover, quasiparticle bursts can cause correlated errors among distant qubits^{7–10}, which can require increased overhead to implement quantum error correction¹¹. Quasiparticle mitigation can be achieved via gap-engineering techniques^{12–14}, which can keep quasiparticles away from the qubit's junctions, confining them in regions with lower superconducting gap. Recent research highlighted intrinsic gap-engineering effects in gap-asymmetric Josephson junctions^{15,16}: in standard nanofabricated Al-AlOx-Al Josephson junctions, the top layer has a larger thickness than the bottom one to ensure the continuity of the film, resulting in a gap asymmetry $\delta\Delta$ due to the strong thickness modulation of the Al superconducting gap below 100 nm. In typical devices, the gap-asymmetry frequency $\omega_{LR}/2\pi = \delta\Delta/(2\pi\hbar)$ (\hbar is the reduced Planck's constant, which we set to unity from now on) can be of the order of a few GHz, and is thus comparable, or even exceeding, the qubit frequency $\omega_{10}/2\pi$. In fact, qubits fabricated with $\omega_{LR} > \omega_{10}$ are protected from quasiparticle tunneling, as quasiparticles are trapped in the low-gap electrode¹⁶; the advantage of this design was experimentally confirmed in a

3D transmon¹⁷, and it has also been proven effective in suppressing correlated errors in multi-qubit devices¹⁸.

From a complementary point of view, the accurate characterization of superconducting qubits has enabled detailed studies of physical effects that are, in general, more difficult to investigate in other setups: evidence for quasiparticle interference has been reported in T_1 measurements of a fluxonium¹⁹; trapping of quasiparticle by one or more vortices has been measured in a transmon²⁰; higher harmonics in the current-phase relation have been shown to have an influence on the energy level and charge dispersion in transmons larger than naively expected for tunnel junctions²¹. In contrast, while the gap asymmetry itself can be directly extracted from transport measurements²², it is not so easily estimated in qubits; still, its presence leads to a peak in transition rates of a SQUID transmon¹⁵, or to thermal activation of the rates when $k_B T \sim \delta\Delta$ (where T is the temperature and k_B is the Boltzmann constant). In the latter work, the thermal activation behavior is considered as a signature of the coexistence between an excess quasiparticle number and Fermi-like energy distribution of the quasiparticles. Here we extend the low temperature ($k_B T \ll \omega_{LR}, \omega_{10}$) modeling of qubit-quasiparticle interaction¹⁶ to cover the intermediate temperature range up to $k_B T \lesssim \omega_{LR}, \omega_{10}$. With our approach, we can address the temperature dependence of the quasiparticle density, and we show that different nonequilibrium regimes can be possible, depending on the gap asymmetry and the quasiparticle generation rates. We discuss possible limitations of what we call global quasiequilibrium modeling, which may result in an

¹Quantum Research Center, Technology Innovation Institute, Abu Dhabi, UAE. ²JARA Institute for Quantum Information (PGI-11), Forschungszentrum Jülich, Jülich, Germany. ✉e-mail: giampiero.marchegiani@tii.ae

inaccurate estimate of the qubit's parameters, and explore possible measurement schemes to overcome them, in particular exploiting the Fraunhofer effect^{23,24} in the presence of a magnetic field parallel to the junction plane.

Results

Model

For typical qubits based on Al-AlOx-Al Josephson junctions, the qubit transition rates can usually be measured from the base temperature of the dilution refrigerator, $T \sim 10$ mK, up to roughly 250 mK; at this temperature, nonequilibrium effects are expected to be negligible and the qubit's lifetime is usually too short to be of practical interest. In this range the condition $k_B T \ll \Delta$ is well satisfied for aluminum thin film, characterized by a critical temperature $T_C = \Delta/(1.764k_B) \sim 1.6$ K, [here we use the standard relation between the critical temperature and the zero-temperature gap Δ in the Bardeen-Cooper-Schrieffer (BCS) theory²⁵]. Thus, we can safely disregard gap suppression effects due to temperature. We consider a superconducting qubit comprising a single Josephson junction (JJ), i.e., two superconducting films, denoted with left (L) and right (R), separated by a thin, nanometer-scale insulating barrier. Unless explicitly specified, we set $k_B = 1$ hereinafter. We aim to describe the evolution with temperature of the qubit-quasiparticle system, incorporating nonequilibrium effects. Specifically, we consider the following ansatz for the quasiparticle energy distributions in the left (f_L) and right (f_R) electrodes forming the Josephson junction,

$$f_L(\epsilon) = f_0(\epsilon - \mu_L), \quad (1)$$

$$f_R(\epsilon) = f_0(\epsilon - \mu_{R<})\theta(\Delta_L - \epsilon) + f_0(\epsilon - \mu_{R>})\theta(\epsilon - \Delta_L), \quad (2)$$

where ϵ is the quasiparticle energy measured with respect to the Fermi level, $\theta(\epsilon)$ is the Heaviside step function, $f_0(\epsilon) = [\exp(\epsilon/T) + 1]^{-1}$ is the Fermi-Dirac distribution, and T is the quasiparticle temperature. We take the latter to coincide with the phonon temperature of the substrate¹⁷ – we discuss limitations to this assumption in the Discussion section below. We account for the possible nonequilibrium nature of the quasiparticles via the effective chemical potentials μ_L , $\mu_{R<}$, and $\mu_{R>}$ – the equilibrium case being $\mu_L = \mu_{R<} = \mu_{R>} = 0$. In our approach, the chemical potentials will be an output of our model and are determined by the interplay between the different physical processes involving the quasiparticles (detailed in the next subsection). This approach generalizes that pioneered by Owen and Scalapino²⁶, which has already been used in modeling superconducting qubits^{27–29}. In Fig. 1, we give a schematic representation of our ansatz. Specifically, we display the quasiparticle density of states (DoS) in the two superconducting electrodes of the JJ, characterized by the energy gaps Δ_L and Δ_R ; with no loss of generality, we assume $\Delta_L \geq \Delta_R$ hereinafter. The quasiparticle distributions are represented via filled curves: the darker regions correspond to occupied states, while the lighter fillings characterize unavailable states. The occupation of states with energy larger than the chemical potential is exponentially suppressed with the ratio $(\epsilon - \mu)/T$, as per our ansatz [cf. Eqs. (1) and (2)]. We remark that the three chemical potentials are, in general, different; in Fig. 1a, we consider a specific order, i.e., $\mu_L > \mu_{R>} > \mu_{R<}$ which can occur at low temperature (see “Chemical potentials vs temperature” subsection). In Fig. 1b the low-gap electrode is characterized by a single chemical potential, $\mu_{R>} = \mu_{R<} \neq \mu_L$ (local quasiequilibrium), while in Fig. 1c the three chemical potentials are the same, a situation which we call global quasiequilibrium. For reference, we show with a dashed line the quasiparticle distribution in the left electrode at equilibrium, $\mu_L = 0$.

Rate equations

Since in this work we investigate the nonequilibrium steady state of the quasiparticle-qubit system in the absence of any coherent drive, we can simply focus on the diagonal part of the density matrix, whose dynamics is

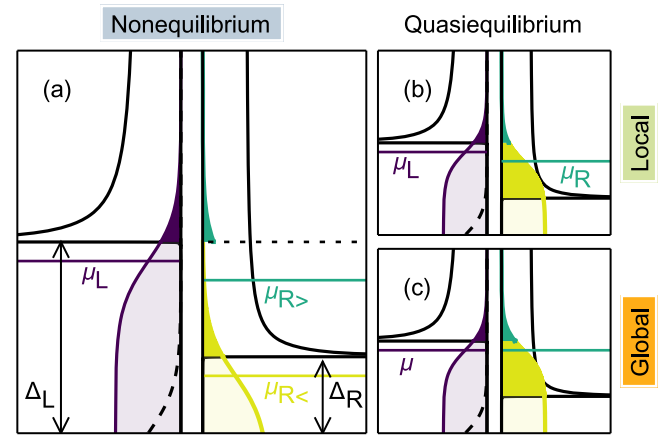


Fig. 1 | Schematic of different nonequilibrium regimes. In each panel we show the density of states and quasiparticle distribution functions in the two superconducting electrodes forming the Josephson junction of a transmon qubit. The two electrodes are characterized by a gapped excitation spectrum with asymmetric gaps, $\Delta_L > \Delta_R$. We consider Fermi distributions with characteristic temperature T corresponding to the phonon bath temperature. The excess quasiparticle density in the high-gap electrode is accounted for through a chemical potential μ_L (at thermal equilibrium, the chemical potential coincides with the Fermi energy, $\mu_L = 0$). In the right electrode, we distinguish between excitations with energy smaller or larger than Δ_L : correspondingly, we identify two different values for the chemical potential, $\mu_{R>}$ and $\mu_{R<}$. The different regimes are: **a** full nonequilibrium **b** local quasiequilibrium ($\mu_{R>} = \mu_{R<} \neq \mu_L$), and **c** global quasiequilibrium ($\mu_{R>} = \mu_{R<} = \mu_L$).

governed by rate equations. When dephasing effects need to be considered, a more general approach is required^{28,30}. We consider low temperatures compared to the gap; more precisely, we assume $T \ll \Delta - \mu$, so the quasiparticle occupation probability is small, $f_L, f_R \ll 1$. Thus, we can equivalently consider the quasiparticle densities x_L , $x_{R<}$, and $x_{R>}$ ¹⁶, which are in one-to-one correspondence with the chemical potentials (the relation is given in Supplementary Note I). This choice is convenient since, with our assumption, the rates of transition between qubit states induced by quasiparticles are proportional to their densities, and it eases comparison with previous literature⁵. We define $x_{R>} (x_{R<})$ as the quasiparticle density in the low-gap electrode with energy larger (smaller) than Δ_L ¹⁶.

The rate equations for the occupation probability p_i of the qubit logical state i (with $\bar{i} = 1$ for $i = 0$ and vice versa) read

$$\dot{p}_i = -(\Gamma_{ii}^{eo} + \Gamma_{ii}^{ee})p_i + (\Gamma_{\bar{i}\bar{i}}^{eo} + \Gamma_{\bar{i}\bar{i}}^{ee})p_{\bar{i}}, \quad (3)$$

where the dot denotes the time derivative and we explicitly distinguish between rates preserving and changing the parity ($e = \text{even}$ and $o = \text{odd}$); here the parity is that of the number of quasiparticles that have tunneled across the junction^{5,28} and we assume the rates to be symmetric when exchanging parities, $e \leftrightarrow o$, see Supplementary Note II. Parity-preserving rates are of non-quasiparticle origin; in this work we assume that such transitions are caused by a thermal bath and hence, according to the detailed balance principle, we have $\Gamma_{01}^{ee} = \exp(-\omega_{10}/T)\Gamma_{10}^{ee}$. In contrast, rates modifying the parity are related to quasiparticle events; they can be expressed as $\Gamma_{ii}^{eo} = \Gamma_{ii}^{\text{ph}} + \sum_{\alpha} \tilde{\Gamma}_{ii}^{\alpha} x_{\alpha}$, where Γ_{ii}^{ph} accounts for photon-assisted transition³¹; these transitions are caused by pair-breaking photons and contribute to quasiparticle generation (see the “Quasiparticle generation mechanisms” subsection). In the sum, $\alpha = \{L, R>, R<\}$ denotes the initial location of the quasiparticle tunneling through the junction.

The rate equations for x_L , $x_{R>}$, $x_{R<}$ were introduced and discussed in detail in the low-temperature limit $T \ll \omega_{10}, \omega_{LR}, |\omega_{10} - \omega_{LR}|$ ¹⁶; here, we present them in a slightly generalized form to incorporate physical processes

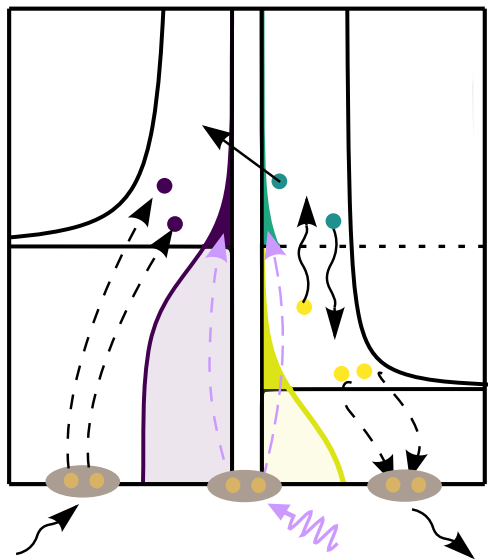


Fig. 2 | Processes governing the quasiparticle dynamics. The upward diagonal arrow represents a qubit relaxation event in which a quasiparticle tunnels from the right to the left electrode. Wavy arrows denote phonon-mediated processes: the downward arrow shows a quasiparticle relaxation process accompanied by phonon emission, while the upward one excitation by phonon absorption. Phonons can also break Cooper pairs (see bottom of left electrode), or be emitted in a recombination event (see right electrode). Pair-breaking photons lead to generation of one quasiparticle in each electrode at the same time.

that become important for temperatures comparable to the other three energy scales:

$$\begin{aligned} \dot{x}_L &= g^L - r^L x_L^2 - \delta \left[(\bar{\Gamma}_{00}^L + \bar{\Gamma}_{01}^L) p_0 + (\bar{\Gamma}_{11}^L + \bar{\Gamma}_{10}^L) p_1 \right] x_L \\ &\quad + \delta \bar{\Gamma}_{10}^{R<} p_1 x_{R<} \\ &\quad + \delta \left[(\bar{\Gamma}_{00}^{R>} + \bar{\Gamma}_{01}^{R>}) p_0 + (\bar{\Gamma}_{11}^{R>} + \bar{\Gamma}_{10}^{R>}) p_1 \right] x_{R>} , \end{aligned} \quad (4)$$

$$\begin{aligned} \dot{x}_{R>} &= g^{R>} - r^{R>} x_{R>}^2 - r^{<} x_{R<} x_{R>} \\ &\quad - \left[(\bar{\Gamma}_{00}^{R>} + \bar{\Gamma}_{01}^{R>}) p_0 + (\bar{\Gamma}_{11}^{R>} + \bar{\Gamma}_{10}^{R>}) p_1 \right] x_{R>} \\ &\quad + \left[\bar{\Gamma}_{00}^L p_0 + (\bar{\Gamma}_{11}^L + \bar{\Gamma}_{10}^L) p_1 \right] x_L + \xi \bar{\Gamma}_{01}^L p_0 x_L \\ &\quad - \tau_R^{-1} x_{R>} + \tau_E^{-1} x_{R<} , \end{aligned} \quad (5)$$

$$\begin{aligned} \dot{x}_{R<} &= g^{R<} - r^{R<} x_{R<}^2 - r^{<} x_{R<} x_{R>} - \bar{\Gamma}_{10}^{R<} p_1 x_{R<} \\ &\quad + (1 - \xi) \bar{\Gamma}_{01}^L p_0 x_L + \tau_R^{-1} x_{R>} - \tau_E^{-1} x_{R<} , \end{aligned} \quad (6)$$

where the gap ratio $\delta = \Delta_R/\Delta_L$ in Eq. (4) is related to our normalization choice of the quasiparticle densities (see Supplementary Note I), which differs from the one made elsewhere¹⁷. The quasiparticles processes which we discuss next are schematically summarized in Fig. 2. In the right-hand side (RHS) of Eqs. (4)–(6), terms associated with a positive sign increase the quasiparticle density, while terms with a negative sign reduce the density. The total quasiparticle number in the device is $N_{qp} = 2\nu_0\Delta_L\mathcal{V}[x_L + \delta(x_{R<} + x_{R>})]$, where we assumed for simplicity the single-spin densities of states at the Fermi level in each electrode $\nu^L = \nu^R = \nu_0$ as well as the electrodes' volumes $\mathcal{V}_L = \mathcal{V}_R = \mathcal{V}$ to be the same. The total quasiparticle number can be increased via quasiparticle generation, see terms g^L , $g^{R<}$, and $g^{R>}$ (see discussion in the “Quasiparticle generation mechanisms” subsection), or reduced via quasiparticle recombination. The latter mechanism destroys two quasiparticles either in the left [term proportional to r^L in the RHS of Eq. (4)] or in the right [terms proportional to $r^{>}$, $r^{R>}$ and $r^{R<}$ in the RHS of Eqs. (5) and (6)] electrode, with consequent

phonon emission. Terms linear in the densities do not change the total quasiparticle number; rather, they lead to a redistribution of these excitations. In the low-gap electrode, electron-phonon scattering can lead to quasiparticle excitation and relaxation [terms $\tau_E^{-1}x_{R<}$ and $\tau_R^{-1}x_{R>}$ in the RHS of Eqs. (5) and (6), respectively]. The remaining terms are associated with quasiparticle tunneling; these processes always change the qubit’s parity ($e \rightarrow o$ or $o \rightarrow e$) and can lead to a transition between initial (*i*) and final (*f*) qubit logical states. In the rate equations, they appear in a specific combination of the general form $\bar{\Gamma}_{ij}^\alpha p_i x_\alpha$, where the quantity $\bar{\Gamma}_{ij}^\alpha$ is the tunneling rate for a single quasiparticle (a different notation is used in other works^{15,17}). These rates correspond to the tilde rates in $\tilde{\Gamma}_{ii}^\alpha$ [see Eq. (3) and text that follows] divided by the Cooper pair number in the low-gap electrode, i.e., $\bar{\Gamma}_{if}^\alpha = \tilde{\Gamma}_{if}^\alpha / (2\nu_0\Delta_R\mathcal{V})$ ¹⁶. The rates $\bar{\Gamma}_{ii}^{R<}$, $\bar{\Gamma}_{01}^{R<}$ are exactly zero due to our ansatz in Eqs. (1) and (2). The p_i factors in Eqs. (4)–(6) and the dependence of the rates entering in Eq. (3) on the quasiparticle densities couple the dynamics of the qubit and the quasiparticles. Below, we solve these equations in the steady state as a function of quasiparticle temperature for typical experimental parameters, and we identify various nonequilibrium regimes.

Explicit expressions for the rates and their temperature dependence in terms of qubit parameters in the case of a transmon are given in Supplementary Note III. Here we comment on the relation between the above rates equations with those in the low-temperature limit¹⁶. The dimensionless factor $0 \leq \xi \leq 1$ denotes the fraction of quasiparticles tunneling from the left to the right electrode with final quasiparticle energy larger than Δ_L in a qubit excitation process (see Supplementary Note III D), and it is, in general, a function of T , ω_{LR} , and ω_{10} ; at low temperature $T \ll |\omega_{10} - \omega_{LR}|$, ξ is exponentially suppressed as $e^{-\min(\omega_{LR}, \omega_{10})/T}$. The quasiparticle excitation rate τ_E^{-1} due to thermal phonons is exponentially small in ω_{LR}/T (see Supplementary Note IV) and was thus disregarded in the low-temperature modeling¹⁶. Finally, the rate $\bar{\Gamma}_{01}^{R>} \propto e^{-\omega_{10}/T}$ is also exponentially suppressed (see Supplementary Note III). Hence, in the low-temperature limit $T \ll \omega_{10}$, ω_{LR} , $|\omega_{LR} - \omega_{10}|$, the Eqs. (4)–(6) reduce to those in the literature¹⁶. The generalization given here, as we show below, enables us to study the crossover to full equilibrium.

Quasiparticle generation mechanisms

Quasiparticles are generated by pair-breaking processes due to the interaction of the electrons in the superconductors forming the junction with phonons in the electrodes and with external electromagnetic radiation³². Thus, we express the generation rate for the quasiparticle density x_α (with $\alpha = \{L, R<, R>\}$) as the sum of PHotons and PhoNons contributions

$$g^\alpha = g_\alpha^{\text{ph}} + g_\alpha^{\text{pn}} . \quad (7)$$

Nonequilibrium quasiparticle effects in superconducting qubits and resonators due to the interplay between phonons and photons have previously been investigated^{33,34}, and more recently including photon pair-breaking processes³⁵. In this work, we assume that the photon absorption mainly occurs at the junction due to its high impedance with respect to the rest of the circuit³⁶. Absorption of photons with energy ω_v larger than the gap sum $\Delta_L + \Delta_R$ causes photon-assisted tunneling processes³¹, leading both to quasiparticle generation and parity switching. The generation rate by pair-breaking photons in electrode $\alpha = \{L, R\}$ is obtained by dividing the total photon-assisted rate $\Gamma^{\text{ph}} = \sum_{i,j,p_i} \bar{\Gamma}_{ij}^{\text{ph}}$ by the Cooper pair number in α , i.e., $g_R^{\text{ph}} = \Gamma^{\text{ph}} / (2\nu_0\Delta_R\mathcal{V}) = g_L^{\text{ph}} / \delta$ (the δ at the denominator is related again to our normalization choice¹⁶); the separation of g_R^{ph} into generation rates for quasiparticles with energy smaller ($g_{R<}^{\text{ph}}$) and larger ($g_{R>}^{\text{ph}}$) than Δ_L and expressions for $\bar{\Gamma}_{ij}^{\text{ph}}$ are discussed in Supplementary Note V.

Phonon absorption mainly occurs in the bulk, and lead to quasiparticle generation in electrode $\alpha = \{L, R\}$ above the energy threshold $2\Delta_\alpha$. Recent works have shown that pair-breaking phonons generated by absorption of background radiation can threaten the operation of superconducting qubits^{7,37–39}. Such radiation can lead to quasiparticle bursts and so a temporary increase in the quasiparticle density^{8,39,40}; the precise description of

this time-resolved dynamics⁴¹ goes beyond the scope of this manuscript. Hence, in this work, we disregard quasiparticle generation due to nonequilibrium phonons, which can also be suppressed using phonon traps^{42,43}. Conversely, since we are primarily interested in discussing the evolution with temperature of the quasiparticle-qubit system, we include the contribution of thermal phonons, and express the generation rates by phonons as $g_L^{\text{pn}} = 2\pi r^L T e^{-2\Delta_L/T}/\Delta_L$, $g_{R<}^{\text{pn}} = 2\pi r^{R<} T e^{-2\Delta_R/T} \text{erf}[\sqrt{\omega_{LR}/T}]/\Delta_R$, $g_{R>}^{\text{pn}} = 2\pi r^{R>} T e^{-2\Delta_R/T} \text{erfc}[\sqrt{\omega_{LR}/T}]/\Delta_R$; these expressions are valid for $T \ll \Delta_L, \Delta_R$, see Supplementary Note IV D.

Chemical potentials vs temperature

Having introduced our models for the coupled quasiparticle-qubit system, we now move to considering its steady state as function of temperature T . In this case, the time derivatives on the left-hand sides of Eqs. (3)–(6) vanish, and those equations reduce to algebraic ones. Still, the system being nonlinear, analytical solutions can only be found approximately in certain limits, as we discuss in Supplementary Note VI. Here, we numerically find the roots of the system of coupled equations; subsequently, we calculate the chemical potentials μ_L , $\mu_{R>}$, and $\mu_{R<}$ using the computed steady-state values of the quasiparticle densities (cf. Supplementary Note I). In Fig. 3, we display our results for the cases of small $\omega_{LR}/(2\pi) = 0.5$ GHz (panel a) and large gap asymmetry $\omega_{LR}/(2\pi) = 5$ GHz (panel b) in relation to thermal energy $T/(2\pi) = 0.2$ GHz at the base temperature of a typical dilution refrigerator, $T \approx 10. In the calculation, we set the photon-assisted parity-switching rate in the qubit ground state to $\Gamma_{00}^{\text{ph}} = 300, comparable to the values reported by several experiments^{24,44–47}, but few orders of magnitudes larger than that in state-of-the-art devices optimized to suppress such contributions^{17,41,43,48}. Other parameters are specified in the caption. In both cases, all three chemical potentials are the largest at the lowest temperature considered and decrease monotonically (approximately linearly), reaching zero, i.e., full equilibrium, around $T \gtrsim 150$ mK for our parameter choice. This behavior arises from the competition between photon-assisted pair-breaking, which is temperature-independent, and pair-breaking by thermal phonons, whose rate increases exponentially with temperature. Since $\Delta_R < \Delta_L$, a crossover temperature \bar{T} can be defined by comparing photon generation to thermal phonon generation in the right electrode, $g_{R>}^{\text{pn}} + g_{R<}^{\text{pn}} = g_R^{\text{ph}}$, leading to the expression³⁵$$

$$\bar{T} = \frac{2\Delta_R}{W\left(\frac{2\Delta_R}{4\pi r^{R<} / g_R^{\text{ph}}}\right)}, \quad (8)$$

where $W(z)$ is the Lambert W (or product-log) function. For our parameters, this formula provides an estimate of the crossover within a few percent of the numerical results in Fig. 3, as shown by the dashed vertical lines in the figure.

The approximately linear decrease of the chemical potentials with temperature signals a roughly constant quasiparticle density for temperatures below \bar{T} , since $\mu_\alpha \approx \Delta_\alpha - T \log(1/x_\alpha)$ (with a slight abuse of notation, we mean here $\Delta_{R<} \equiv \Delta_{R>} \equiv \Delta_R$); this linear decrease is displayed for $\alpha = R <$ in Fig. 3a, b with dot-dashed lines. Below we comment on the deviation from approximately linear behavior for $\mu_{R>}$ at large gap asymmetry; in fact, the relation between the chemical potentials depends on the gap asymmetry, reflecting different energy distributions in the two cases. For a small ω_{LR} , the nonequilibrium quasiparticles are approximately equally distributed in the two electrodes, $x_L \approx x_{R>} + x_{R<} \approx \sqrt{g_R^{\text{ph}}/r^L}$. At larger ω_{LR} , quasiparticles accumulate in the low-gap electrode, $x_{R<} \gg x_L \gg x_{R>}$, due to fast relaxation compared to tunneling¹⁶. In both cases, the chemical potential differences (see insets of Fig. 3a, b) are largest at the lowest temperature considered, where $\mu_L - \mu_{R>} \sim \mu_{R>} - \mu_{R<} \sim \omega_{LR}$ (slightly greater or smaller than ω_{LR} for small and large gap asymmetry, respectively; see also Supplementary Note I A), and drop as quasiparticle-phonon scattering rates increase with temperature. Hence, at low asymmetry, the chemical potential

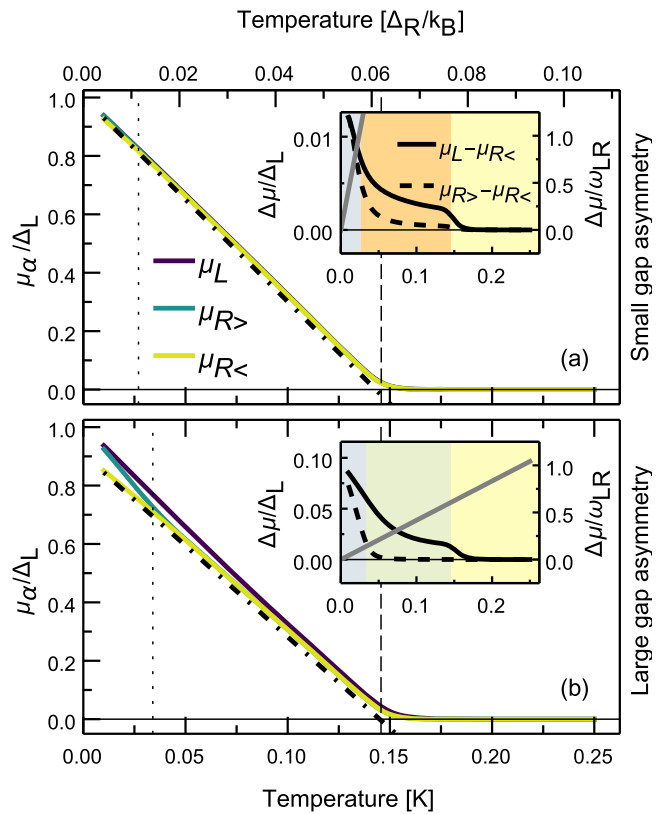


Fig. 3 | Chemical potentials vs temperature. Temperature dependence of the chemical potentials μ_L , $\mu_{R>}$, and $\mu_{R<}$ (cf. Fig. 1a) in a single-junction transmon (charging energy E_C and Josephson energy E_J): a small ($\omega_{LR}/2\pi = 0.5$ GHz) or b large ($\omega_{LR}/2\pi = 5$ GHz) gap asymmetry. The dot-dashed lines represent constant quasiparticle density, as discussed in the “Chemical potentials vs temperature” subsection. Insets: chemical potential differences ($\Delta\mu$) vs temperature. The gray solid lines show the thermal energy for comparison. Note the two scales on the left and the right vertical axis are normalized with the left electrode gap Δ_L and the gap asymmetry ω_{LR} , respectively. Colored regions identify the different regimes: nonequilibrium (aquamarine, left), global quasiequilibrium (orange, middle) or local quasiequilibrium (light green, middle), and equilibrium (yellow, right) -- see also the highlighted labels in Fig. 1. The temperature values separating the regimes are identified with dotted and dashed vertical lines in the main panels. Parameters: $\Delta_R/h = 49$ GHz, $\omega_1/h = 5.5$ GHz, $E_J/h = 14.5$ GHz, $E_C/h = 290$ MHz, $\omega_r/2\pi = 119$ GHz, $\Gamma_{00}^{\text{ph}} = 300$ Hz, $v_0 = 0.73 \times 10^{47} \text{ J}^{-1} \text{ m}^{-3}$, $V = 506 \times 240 \times 0.028 \mu\text{m}^3$, $\Gamma_{10}^{\text{ee}} = 100$ kHz, $r^L = r^{R<} = 6.25$ MHz.

differences become smaller than the thermal energy (solid gray line in Fig. 3a) already at low temperature, and the system is approximately in global quasiequilibrium (see also the “Impact on qubit transition rates” subsection). In contrast, the chemical potential differences can remain above the thermal energy up to higher temperatures in the gap-asymmetric case. This makes it possible to clearly identify different regimes: for $T \lesssim 30$ mK the three chemical potentials are unequal $\mu_L > \mu_{R>} > \mu_{R<}$ (the nonequilibrium regime of Fig. 1a); for 30 mK $\lesssim T \lesssim \bar{T} \simeq 150$ mK the low-gap electrode can be characterized using a single chemical potential, $\mu_{R>} = \mu_{R<} \neq \mu_L$ (local quasiequilibrium, Fig. 1b); finally, above \bar{T} the three chemical potentials fully equilibrate, $\mu_{R>} \approx \mu_{R<} \approx \mu_L \ll T$. The transition between nonequilibrium and local quasiequilibrium and the corresponding deviation from linearity for $\mu_{R>}$ vs T are due to the interplay between tunneling from the high-gap to the low-gap electrode and the excitation rate due to phonon absorption in the low-gap electrode: at sufficiently low temperatures, quasiparticle excitations is slow compared to tunneling, leading to a nonequilibrium accumulation in the low gap-electrode, $\mu_{R>} > \mu_{R<}$; as the temperature increases, the excitation rate grows exponentially with temperature, becomes faster than tunneling, and we have $\mu_{R>} \approx \mu_{R<} \approx \mu_L$.

approaching $\mu_{R<}$ (see Supplementary Note VI D). The dotted vertical lines in Fig. 3a, b identify the temperature at which the tunneling from the left to the right electrode at energies $\epsilon \geq \Delta_L$ equates the excitation rate (see Supplementary Note VI D); below this temperature we have the nonequilibrium regions (aquamarine) highlighted in the insets.

Impact on qubit transition rates

The measurement of parity-switching rates is well-established as a probe of quasiparticle effects^{28,45,49}, so we consider now whether such measurements can help distinguishing the various nonequilibrium regimes. In Fig. 4a we display the parity switching rate $\Gamma_P = p_0(\Gamma_{01}^{eo} + \Gamma_{00}^{eo}) + p_1(\Gamma_{10}^{eo} + \Gamma_{11}^{eo})$ calculated using the same parameters as in Fig. 3 (solid curves). The parity-switching rate increases monotonically for the large-asymmetry junction, while for the small-asymmetry one there is a nonmonotonic evolution at low temperatures $T \lesssim 25$ mK. This nonmonotonic behavior stems from the competition between the tunneling rate $\bar{\Gamma}_{00}^{R>}$ and relaxation in the low-gap electrode (τ_R^{-1}), favoring the accumulation of quasiparticles at energies above Δ_L when temperature becomes smaller than the gap difference (see Supplementary Notes III and VI). This interplay is absent for large gap-asymmetries, since relaxation is fast compared to tunneling $\tau_R^{-1} \gg \bar{\Gamma}_{00}^{R>} \text{ }^{16}$, leading to accumulation of quasiparticles at the low-gap energy. For comparison, we also display the parity-switching rates calculated assuming global quasiequilibrium (dashed curves), in which case the ratio between the quasiparticle densities is fixed by the gap asymmetry and the temperature (see last paragraph in Supplementary Note VI) and the overall density by the total generation rate, cf. Eq. (7). For small gap asymmetry, the global quasiequilibrium modeling reproduces accurately the full nonequilibrium calculation, except at the lowest temperatures; the region of agreement coincides with that where the chemical potential differences are smaller than temperature, see inset in Fig. 3a. The low-temperature nonmonotonic feature is missed because by requiring equal chemical potentials the thus constrained model underestimates the number of quasiparticles with energy larger than Δ_L ¹⁶, since in fact we have $\mu_L \approx \mu_{R>} > \mu_{R<}$. However, this discrepancy may be difficult to uncover experimentally, as achieving thermalization is progressively harder closer to the base temperature of the cryostat⁵⁰. For large asymmetry, measurement of Γ_P also does not permit distinguishing global quasiequilibrium from full or local nonequilibrium: the temperature behavior is qualitatively similar, and by repeating the calculation with different photon rate and the gap asymmetry (increased by factors of 2 and ~ 1.2 , respectively, for our parameter choice), the global quasiequilibrium approach can describe reasonably well the results of the full model. Therefore, even though one could fit experimental data for parity lifetime vs temperature assuming global quasiequilibrium, the extracted parameter values would not be accurate.

The analysis above shows that additional measurements are needed to identify the nonequilibrium regimes. One possibility is to consider the temperature dependence of the ratio between excitation and relaxation rates for parity switching transitions, as displayed in Fig. 4b. For this quantity, the difference between the global quasiequilibrium and the full nonequilibrium modeling is hardly noticeable for small gap asymmetry, while more prominent deviations occur for the large-asymmetry junction. Importantly, the deviations become even more significant when the parameters are rescaled as discussed above (cf. Fig. 4a) to capture the total parity lifetime; in other words, it is in general not possible to consistently fit data for both Γ_P and $\Gamma_{10}^{eo}/\Gamma_{10}^{eo}$ under the assumption of global quasiequilibrium. For our specific parameters, the order relation between gap asymmetry and frequency switches from $\omega_{LR} < \omega_{10}$ to $\omega_{LR} > \omega_{10}$ after rescaling. In the latter case the rate $\bar{\Gamma}_{10}^{R<}$ is exponentially suppressed with $(\omega_{LR} - \omega_{10})/T$ (cf. Supplementary Note III C), resulting in the strong upturn of $\Gamma_{01}^{eo}/\Gamma_{10}^{eo}$ at low temperatures. For both small and large asymmetry the excitation/relaxation ratio deviates from the detailed balance expectation $\Gamma_{01}^{eo}/\Gamma_{10}^{eo} = \exp(-\omega_{10}/T)$ (dotted line) because for photon-assisted transitions the excitation and relaxation rates are typically of the same order, $\Gamma_{01}^{ph}/\Gamma_{10}^{ph} \approx 1$ ³¹. In summary, a joint measurement of the parity lifetime and the ratio of the excitation and relaxation rates due to quasiparticles can not only distinguish between full

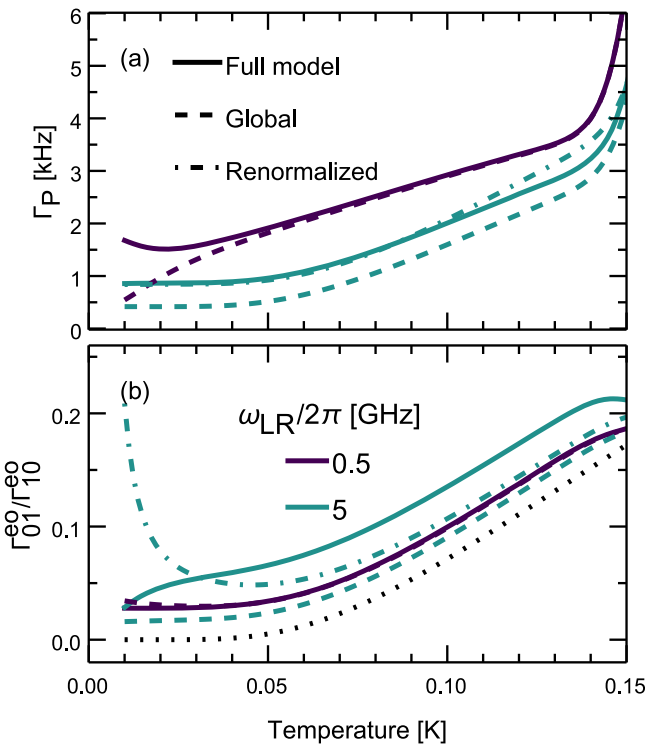


Fig. 4 | Parity-switching rates vs temperature. **a** Total parity-switching rate and **b** excitation to relaxation ratio vs temperature for small and large gap asymmetry (ω_{LR}). Parameters are given in the caption of Fig. 3. For the dot-dashed curves, $\Gamma_{01}^{ph} = 600$ Hz and $\omega_{LR}/(2\pi) = 6$ GHz.

equilibrium and nonequilibrium, but also discriminate different nonequilibrium regimes, at least for large gap asymmetry.

Magnetic field tuning

While the concurrent measurement of excitation/relaxation and parity-switching rates has been demonstrated already⁴⁹, it is more demanding than the determination of just the total parity-switching rate. Measuring the latter together with an accurate estimate of the gap asymmetry ω_{LR} would enable probing the various nonequilibrium regimes. Standard techniques for the measurement of ω_{LR} , such as tunnel spectroscopy, are in general unavailable in qubits, and we estimate the uncertainty in ω_{LR} from quantum transport measurements on previously fabricated devices in the GHz range. In fact, nominally identical superconducting films displays gap variations of the order of a few up to tens of μeV ³¹; at the same time, the determination of ω_{LR} via the so-called “singularity-matching peak” in the current-voltage characteristics²⁵ has some intrinsic limitations, given its reduced visibility for $T \ll T_C$ and the thermal broadening^{52,53}. As quasiparticle tunneling is enhanced near the resonant condition $\omega_{10} = \omega_{LR}$ ¹⁶, tuning on-chip the qubit frequency ω_{10} is a viable strategy for estimating ω_{LR} . The qubit frequency is commonly controlled by applying a magnetic field perpendicular to the plane of the junctions in a two-junction SQUID^{54,55}. In such a setup, it is possible to identify ω_{LR} by measuring the parity lifetime as a function of the perpendicular field; this strategy was successfully adopted in a recent experiment¹⁵, where a peak in the parity-switching rate was observed at the resonant condition. In particular, ω_{LR} was obtained with a resolution in the tens of MHz with this approach, which is suitable for $T \ll T_C$.

An alternative way to tune the qubit frequency that can be used also in single-junction devices consists in applying a relatively strong magnetic field $B_{||}$, with typical values between tens to hundreds of mT for aluminum devices, in the plane of the junction, see schematic of Fig. 5a (the field is hence stronger than those usually applied in the perpendicular direction; nonetheless, transmon qubits have been shown to be resilient to in-plane fields, with lifetimes depending weakly on field up to a few hundred mT²³).

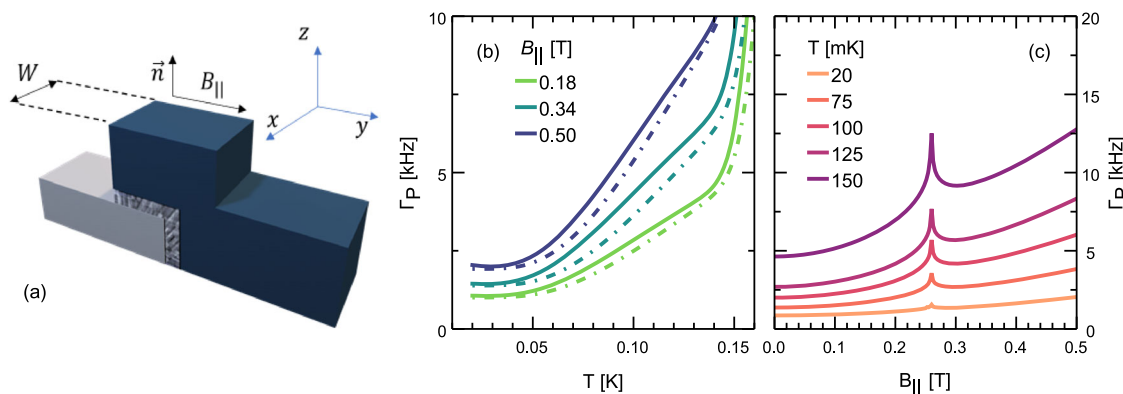


Fig. 5 | Parity-switching rate in parallel magnetic field. **a** Schematic of a Josephson junction with magnetic field B_{\parallel} applied in the plane of the junction, causing a phase gradient along the width W of the junction. **b** Parity-switching rate vs temperature for different in-plane fields. Solid curves are obtained using the full model, while the dot-dashed curves correspond to a global quasiequilibrium modeling with the same

renormalized parameters used to capture the behavior of the zero-field curve (see caption to Fig. 4). **c** Parity-switching rate vs in-plane magnetic field for different temperatures. The rate has a peak, at $B_{\parallel} \approx 0.27$ T, when the resonant condition $\omega_{10}(B_{\parallel}) = \omega_{LR}$ is met. Parameters: $B_{\phi} = 0.8$ T, $\omega_{LR}/(2\pi) = 5$ GHz, and the zero-field values of the remaining parameters are given in the caption of Fig. 3.

The magnetic field modulates ω_{10} by means of two separate effects. First, the field weakens superconductivity in the two electrodes²⁵. The gaps of the two electrodes decrease monotonically with B_{\parallel} , thus reducing ω_{10} (in a transmon, $\omega_{10} \propto \sqrt{E_J}$, and the Josephson energy E_J is approximately proportional to the average gap); moreover, since the critical field for this modulation decreases with the film thickness⁵⁶, the gap of the thicker film is typically suppressed more significantly, thus possibly affecting ω_{LR} . Second, the penetration of the magnetic field through the junction oxide barrier makes the phase difference position dependent, varying along the direction x in Fig. 5a, thus affecting directly the Josephson coupling. More precisely, the critical current of the junction is modulated by the magnetic field in a pattern resembling the Fraunhofer diffraction by a narrow slit (see Supplementary Note VII for more details)²². The device geometry controls the relative size of these two suppression effects: for junctions with sufficiently thin electrodes, as the one experimentally investigated in field-resilient transmons^{23,24}, the frequency suppression is dominated by the Fraunhofer effect up to hundreds of milliTesla, with negligible gap-difference modulations; in practice, one could further reduce the field needed for frequency suppression and hence the field-induced change in ω_{LR} by properly choosing the aspect ratio of the junction (making it wider in the x direction as compared to the y one) while keeping fixed other parameters such as junction area and film thicknesses. For our goals, we assume for simplicity to be in such a regime, so to disregard any change in ω_{LR} due to the magnetic field B_{\parallel} .

Figure 5b displays the parity switching rate as a function of temperature for a few values of the in-plane magnetic field and large gap-asymmetry. The temperature dependence is qualitatively similar to the one already discussed above. Typically, the parity switching rates increase with the magnetic field; the exception is for fields such that $\omega_{10}(B_{\parallel}) \lesssim \omega_{LR}$, as discussed more extensively below. The solid curves are obtained using the full nonequilibrium model, treating the three quasiparticle densities as independent variables, while the dot-dashed curves are obtained assuming a global quasiequilibrium regime and renormalizing the parameters so as to match the zero-field curve, see Fig. 4a. We note that at finite values of the magnetic field, the discrepancy between the full model and the global quasiequilibrium approach extends over a much wider temperature range compared to the zero-field case (cf. Fig. 4a). These results suggest that it is not possible to use a consistent set of parameters to capture both the temperature dependence and the magnetic field dependence of the transition rates within the global quasiequilibrium approach. In other words, measuring the rates at different values of B_{\parallel} is a suitable approach to identify nonequilibrium regimes.

Moreover, the magnetic field evolution of the parity switching rates at a given temperature can give a direct probe of the gap asymmetry. In

Fig. 5c, we display the parity switching rate as a function of the in-plane magnetic field for different temperatures; the dependence of the transition rates on B_{\parallel} is mainly related to interference effects due to the position-dependent phase difference across the junction (see Supplementary Note VII). The parity-switching rate evolution with field qualitatively resembles the behavior observed in a SQUID transmon for perpendicular field up to half-flux quantum¹⁵; the rate typically increases with the field, except in the vicinity of $B_{\parallel} \approx 0.27$ T, where the peak signals again the resonance $\omega_{10} = \omega_{LR}$. As one can no longer “renormalize” the gap difference as to fit the data, the independent determination of ω_{LR} enables distinguishing between global and local quasiequilibrium, since the difference between the two approaches is manifest in the temperature regime for which $\mu_{R>} = \mu_{R<} \neq \mu_L$ (cf. Figs. 3b and 5b).

Discussion

We have developed a model based on rate equations to investigate the evolution with temperature of the qubit-quasiparticle system. Using effective chemical potentials, our model predicts different nonequilibrium regimes. Superconducting qubits with gap asymmetry at most comparable to the thermal energy even at base temperature can largely be described with a single chemical potential, a situation which we call global quasiequilibrium. The competition between quasiparticle generation by pair-breaking photons and thermal phonons results in the commonly observed crossover between the low-temperature limit, where the quasiparticles are out of equilibrium (finite chemical potential), and the high-temperature limit, where quasiparticles are thermalized to the substrate phonons (with vanishing chemical potential).

In transmon with gap-asymmetric junctions, the quasiparticles in the two electrodes can be characterized by two different chemical potentials. This local quasiequilibrium regime can be observed for temperatures smaller than the gap asymmetry at which moreover quasiparticle-phonon scattering is fast enough to enable thermalization in the low-gap electrode. We discussed possible measurement strategies to discriminate the local and the global quasiequilibrium regimes, such as the joint measurement of excitation and relaxation parity-switching rates, or the estimate of these rates for different values of an in-plane magnetic field. Failing to account for the local nonequilibrium regime can result in inaccurate estimates of parameters such as the gap asymmetry and the photon-assisted generation rate. Conversely, the accurate determination of system parameters can be helpful in improving devices in which the precise targeting of parameter values is important, such as multi-qubit chips.

For temperatures at which tunneling is fast compared to quasiparticle-phonon scattering, our model predicts a third nonequilibrium regime with three different chemical potentials (and even a fourth regime with

$\mu_L - \mu_{R>} \lesssim T \ll \mu_L - \mu_{R<}$ for small ω_{LR} , cf. Supplementary Note VI A). However, such prediction is less reliable due to our thermalization ansatz [cf. Eqs. (1) and (2)]. In fact, it is known that $f_L(\epsilon)$ and $f_{R>}(\epsilon)$ can deviate from the Fermi distribution at low temperatures^{33–35}; thus, a more accurate description of this regime requires determining the distribution function $f_L(\epsilon)$ and $f_{R>}(\epsilon)$ as solutions of kinetic equations. The investigation of energy dependence of the quasiparticle distributions is beyond the scope of the present analysis; nevertheless, the estimates for the transition rates should be at least qualitatively correct, since the rates are mainly proportional to the quasiparticle densities (see Supplementary Note III C). Indeed, our modeling has a weak dependence on the quasiparticle temperature T for $T \ll \omega_{LR}, \omega_{10}, |\omega_{10} - \omega_{LR}|$, in agreement with previous work¹⁶. We remark that our notion of quasiequilibrium differs from the one commonly used for charge and heat transport in normal-metal and superconducting junctions^{50,57}. In those experiments, the electron-electron scattering rate is fast compared to the electron-phonon one, and a thermal gradient between the quasiparticle and the phonon systems can be established. In superconductors, this regime can be realized if a large fraction of Cooper pairs is broken (that is, if the normalized densities x_α are not too small), as is generally the case for temperatures not too low compared to the critical one. Here we have considered parameter regimes in which the quasiparticle densities and temperatures are low ($x_\alpha \ll 1$ and $T \ll T_C$); then the quasiparticle-phonon scattering is typically faster than that due to quasiparticle-quasiparticle interaction^{58,59}, and so the latter can be ignored (cf. Supplementary Note IV).

In this work we have neglected any mechanism leading to quasiparticle trapping. Quasiparticles can be trapped away from the junction through gap-engineering techniques, such as controlling the film thickness during deposition¹² or by adding normal-metal¹⁴ or superconducting traps⁶⁰. Quasiparticles can also be trapped in the core of vortices which can be present in a device because of residual magnetic fields²⁰. Phenomenologically, trapping can be incorporated in our rate equations by adding negative terms proportional to the densities to the right-hand sides of Eqs. (4)–(6)¹⁶ and could lead to additional nonequilibrium regimes in which the relations $\mu_L \geq \mu_{R>} \geq \mu_{R<}$ may be violated. The proper inclusion of one or more trapping processes is left to future research.

Methods

The steady-state values of the quasiparticle densities have been obtained by setting to zero the left hand side of the rate equations Eq. (4)–(6). The solution to this nonlinear algebraic system of equations has been found using standard findroot algorithms. The numerical results have been benchmarked with the analytical approximations derived in limiting cases.

Data availability

The datasets used and analyzed in this paper are available from the corresponding author upon reasonable request.

Code availability

The code used to generate the data for this paper is available from the corresponding author upon reasonable request.

Received: 25 October 2024; Accepted: 18 March 2025;

Published online: 27 March 2025

References

- Kjaergaard, M. et al. Superconducting qubits: current state of play. *Annu. Rev. Condens. Matter Phys.* **11**, 369 (2020).
- Siddiqi, I. Engineering high-coherence superconducting qubits. *Nat. Rev. Mater.* **6**, 875 (2021).
- Catelani, G. et al. Quasiparticle relaxation of superconducting qubits in the presence of flux. *Phys. Rev. Lett.* **106**, 077002 (2011).
- Catelani, G., Schoelkopf, R. J., Devoret, M. H. & Glazman, L. I. Relaxation and frequency shifts induced by quasiparticles in superconducting qubits. *Phys. Rev. B* **84**, 064517 (2011).
- Glazman, L. I. & Catelani, G. Bogoliubov Quasiparticles in superconducting qubits. *SciPost Phys. Lect. Notes* **31**, <https://doi.org/10.21468/SciPostPhysLectNotes.31> (2021).
- Papić, M., Tuorila, J., Auer, A., de Vega, I. & Hosseinkhani, A. Charge-parity switching effects and optimisation of transmon-qubit design parameters. *npj Quantum Inf.* **10**, 69 (2024).
- Wilen, C. D. et al. Correlated charge noise and relaxation errors in superconducting qubits. *Nature* **594**, 369 (2021).
- McEwen, M. et al. Resolving catastrophic error bursts from cosmic rays in large arrays of superconducting qubits. *Nat. Phys.* **18**, 107 (2022).
- Li, X.-G. et al. Direct evidence for cosmic-ray-induced correlated errors in superconducting qubit array <https://arxiv.org/abs/2402.04245> (2024), arXiv:2402.04245 [quant-ph].
- Harrington, P. M. et al. Synchronous detection of cosmic rays and correlated errors in superconducting qubit arrays <https://arxiv.org/abs/2402.03208> (2024), arXiv:2402.03208 [quant-ph].
- Xu, Q. et al. Distributed quantum error correction for chip-level catastrophic errors. *Phys. Rev. Lett.* **129**, 240502 (2022).
- Aumentado, J., Keller, M. W., Martinis, J. M. & Devoret, M. H. Nonequilibrium quasiparticles and 2e periodicity in single-cooper-pair transistors. *Phys. Rev. Lett.* **92**, 066802 (2004).
- Sun, L. et al. Measurements of quasiparticle tunneling dynamics in a band-gap-engineered transmon qubit. *Phys. Rev. Lett.* **108**, 230509 (2012).
- Riwar, R.-P. et al. Normal-metal quasiparticle traps for superconducting qubits. *Phys. Rev. B* **94**, 104516 (2016).
- Diamond, S. et al. Distinguishing parity-switching mechanisms in a superconducting qubit. *PRX Quantum* **3**, 040304 (2022).
- Marchegiani, G., Amico, L. & Catelani, G. Quasiparticles in superconducting qubits with asymmetric junctions. *PRX Quantum* **3**, 040338 (2022).
- Connolly, T. et al. Coexistence of nonequilibrium density and equilibrium energy distribution of quasiparticles in a superconducting qubit. *Phys. Rev. Lett.* **132**, 217001 (2024).
- McEwen, M. et al. Resisting high-energy impact events through gap engineering in superconducting qubit arrays. *Phys. Rev. Lett.* **133**, 240601 (2024).
- Pop, I. M. et al. Coherent suppression of electromagnetic dissipation due to superconducting quasiparticles. *Nature* **508**, 369 (2014).
- Wang, C. et al. Measurement and control of quasiparticle dynamics in a superconducting qubit. *Nat. Commun.* **5**, 5836 (2014).
- Willsch, D. et al. Observation of Josephson harmonics in tunnel junctions. *Nat. Phys.* **20**, 815 (2024).
- Barone, A. & Paternò, G. *Physics and applications of the Josephson effect* (Wiley, 1982).
- Krause, J. et al. Magnetic field resilience of three-dimensional transmons with thin-film Al/AIO_x/Al Josephson junctions approaching 1 T. *Phys. Rev. Appl.* **17**, 034032 (2022).
- Krause, J. et al. Quasiparticle effects in magnetic-field-resilient three-dimensional transmons. *Phys. Rev. Appl.* **22**, 044063 (2024).
- Tinkham, M. *Introduction to Superconductivity* (Dover Publications, 2004).
- Owen, C. S. & Scalapino, D. J. Superconducting state under the influence of external dynamic pair breaking. *Phys. Rev. Lett.* **28**, 1559 (1972).
- Palmer, B. S. et al. Steady-state thermodynamics of nonequilibrium quasiparticles in a Cooper-pair box. *Phys. Rev. B* **76**, 054501 (2007).
- Catelani, G. Parity switching and decoherence by quasiparticles in single-junction transmons. *Phys. Rev. B* **89**, 094522 (2014).
- Ansari, M. H. Rate of tunneling nonequilibrium quasiparticles in superconducting qubits. *Supercond. Sci. Technol.* **28**, 045005 (2015).
- Catelani, G., Nigg, S. E., Girvin, S. M., Schoelkopf, R. J. & Glazman, L. I. Decoherence of superconducting qubits caused by quasiparticle tunneling. *Phys. Rev. B* **86**, 184514 (2012).

31. Houzet, M., Serniak, K., Catelani, G., Devoret, M. H. & Glazman, L. I. Photon-assisted charge-parity jumps in a superconducting qubit. *Phys. Rev. Lett.* **123**, 107704 (2019).
32. Catelani, G. & Pekola, J. P. Using materials for quasiparticle engineering. *Mater. Quantum. Technol.* **2**, 013001 (2022).
33. Catelani, G. & Basko, D. M. Non-equilibrium quasiparticles in superconducting circuits: photons vs. phonons. *SciPost Phys.* **6**, 13 (2019).
34. Fischer, P. & Catelani, G. Nonequilibrium quasiparticle distribution in superconducting resonators: an analytical approach. *Phys. Rev. Appl.* **19**, 054087 (2023).
35. Fischer, P. B. & Catelani, G. Nonequilibrium quasiparticle distribution in superconducting resonators: effect of pair-breaking photons. *SciPost Phys.* **17**, 070 (2024).
36. Liu, C. H. et al. Quasiparticle poisoning of superconducting qubits from resonant absorption of pair-breaking photons. *Phys. Rev. Lett.* **132**, 017001 (2024).
37. Gordon, R. T. et al. Environmental radiation impact on lifetimes and quasiparticle tunneling rates of fixed-frequency transmon qubits. *Appl. Phys. Lett.* **120**, 074002 (2022).
38. Vepsäläinen, A. P. et al. Impact of ionizing radiation on superconducting qubit coherence. *Nature* **584**, 551 (2020).
39. Cardani, L. et al. Reducing the impact of radioactivity on quantum circuits in a deep-underground facility. *Nat. Commun.* **12**, 2733 (2021).
40. Grünhaupt, L. et al. Loss mechanisms and quasiparticle dynamics in superconducting microwave resonators made of thin-film granular aluminum. *Phys. Rev. Lett.* **121**, 117001 (2018).
41. Yelton, E. et al. Modeling phonon-mediated quasiparticle poisoning in superconducting qubit arrays. *Phys. Rev. B* **110**, 024519 (2024).
42. Henriques, F. et al. Phonon traps reduce the quasiparticle density in superconducting circuits. *Appl. Phys. Lett.* **115**, 212601 (2019).
43. Iaia, V. et al. Phonon downconversion to suppress correlated errors in superconducting qubits. *Nat Commun* **13**, 6425 (2022).
44. Serniak, K. et al. Direct dispersive monitoring of charge parity in offset-charge-sensitive transmons. *Phys. Rev. Applied* **12**, 014052 (2019).
45. Ristè, D. et al. Millisecond charge-parity fluctuations and induced decoherence in a superconducting transmon qubit. *Nat Commun* **4**, 1913 (2013).
46. Christensen, B. G. et al. Anomalous charge noise in superconducting qubits. *Phys. Rev. B* **100**, 140503 (2019).
47. Kurter, C. et al. Quasiparticle tunneling as a probe of Josephson junction barrier and capacitor material in superconducting qubits. *njp Quantum Inform.* **8**, 31 (2022).
48. Pan, X. et al. Engineering superconducting qubits to reduce quasiparticles and charge noise. *Nat Commun* **13**, 7196 (2022).
49. Serniak, K. et al. Hot nonequilibrium quasiparticles in transmon qubits. *Phys. Rev. Lett.* **121**, 157701 (2018).
50. Giazotto, F., Heikkilä, T. T., Luukanen, A., Savin, A. M. & Pekola, J. P. Opportunities for mesoscopics in thermometry and refrigeration: physics and applications. *Rev. Mod. Phys.* **78**, 217 (2006).
51. Court, N. A., Ferguson, A. J. & Clark, R. G. Energy gap measurement of nanostructured aluminium thin films for single Cooper-pair devices. *Supercond. Sci. Technol.* **21**, 015013 (2007).
52. Ternes, M. et al. Subgap structure in asymmetric superconducting tunnel junctions. *Phys. Rev. B* **74**, 132501 (2006).
53. Germanese, G., Paolucci, F., Marchegiani, G., Braggio, A. & Giazotto, F. Bipolar thermoelectric josephson engine. *Nat. Nanotechnol.* **17**, 1084 (2022).
54. Krantz, P. et al. A quantum engineer's guide to superconducting qubits. *Appl. Phys. Rev.* **6**, 021318 (2019).
55. Blais, A., Grimsmo, A. L., Girvin, S. M. & Wallraff, A. Circuit quantum electrodynamics. *Rev. Mod. Phys.* **93**, 025005 (2021).
56. Meservey, R. & Tedrow, P. Spin-polarized electron tunneling. *Phys. Rep.* **238**, 173 (1994).
57. Muhonen, J. T., Meschke, M. & Pekola, J. P. Micrometre-scale refrigerators. *Rep. Prog. Phys.* **75**, 046501 (2012).
58. Reizer, M. Y. Effective electron-electron interaction in metals and superconductors. *Phys. Rev. B* **39**, 1602 (1989).
59. Devereaux, T. P. & Belitz, D. Disorder enhancement of quasiparticle lifetimes in superconductors. *J. Low Temp. Phys.* **77**, 319 (1989).
60. Riwar, R.-P. & Catelani, G. Efficient quasiparticle traps with low dissipation through gap engineering. *Phys. Rev. B* **100**, 144514 (2019).

Acknowledgements

We acknowledge L. Amico, C. Dickel, and J. Krause for fruitful discussions. G.C. acknowledges support by the German Federal Ministry of Education and Research (BMBF), funding program “Quantum technologies – from basic research to market”, project QSolid (Grant No. 13N16149).

Author contributions

G.M. developed the model, performed the numerical analysis, and drafted the manuscript. G.C. edited the manuscript, and provided supervision and guidance during the project. All authors contributed to the discussion and interpretation of the results.

Competing interests

The authors declare no competing interests.

Additional information

Supplementary information The online version contains supplementary material available at <https://doi.org/10.1038/s42005-025-02052-x>.

Correspondence and requests for materials should be addressed to Giampiero Marchegiani.

Peer review information *Communications Physics* thanks Yoshiki Sunada and the other, anonymous, reviewer(s) for their contribution to the peer review of this work. A peer review file is available.

Reprints and permissions information is available at <http://www.nature.com/reprints>

Publisher's note Springer Nature remains neutral with regard to jurisdictional claims in published maps and institutional affiliations.

Open Access This article is licensed under a Creative Commons Attribution-NonCommercial-NoDerivatives 4.0 International License, which permits any non-commercial use, sharing, distribution and reproduction in any medium or format, as long as you give appropriate credit to the original author(s) and the source, provide a link to the Creative Commons licence, and indicate if you modified the licensed material. You do not have permission under this licence to share adapted material derived from this article or parts of it. The images or other third party material in this article are included in the article's Creative Commons licence, unless indicated otherwise in a credit line to the material. If material is not included in the article's Creative Commons licence and your intended use is not permitted by statutory regulation or exceeds the permitted use, you will need to obtain permission directly from the copyright holder. To view a copy of this licence, visit <http://creativecommons.org/licenses/by-nc-nd/4.0/>.

© The Author(s) 2025